

A Journal of the Gesellschaft Deutscher Chemiker

Angewandte Chemie

GDCh

International Edition

www.angewandte.org

Accepted Article

Title: Local Oxygen Vacancy-mediated Oxygen Exchange for Active and Durable Acidic Water Oxidation

Authors: Ning Zhang, Xinyi Liu, Haixia Zhong, Wei Liu, Di Bao, Jianrong Zeng, Depeng Wang, Caini Ma, and Xin-bo Zhang

This manuscript has been accepted after peer review and appears as an Accepted Article online prior to editing, proofing, and formal publication of the final Version of Record (VoR). The VoR will be published online in Early View as soon as possible and may be different to this Accepted Article as a result of editing. Readers should obtain the VoR from the journal website shown below when it is published to ensure accuracy of information. The authors are responsible for the content of this Accepted Article.

To be cited as: *Angew. Chem. Int. Ed.* **2025**, e202503246

Link to VoR: <https://doi.org/10.1002/anie.202503246>

RESEARCH ARTICLE

Local Oxygen Vacancy-mediated Oxygen Exchange for Active and Durable Acidic Water Oxidation

Ning Zhang^{a,b,#}, Xinyi Liu^{a,#}, Haixia Zhong^{a,b,*}, Wei Liu^{a,b,*}, Di Bao^a, Jianrong Zeng^c, Depeng Wang^{a,b}, Caini Ma^{a,b}, Xinbo Zhang^{a,b,*}

[a] Dr. N. Zhang, Dr. X. Liu, Prof. H. Zhong, Prof. W. Liu, Prof. D. Bao, D. Wang, C. Ma, Prof. X. Zhang

State Key Laboratory of Rare Earth Resource Utilization

Changchun Institute of Applied Chemistry, Chinese Academy of Sciences

No. 5625, Renmin Street, Chaoyang District, Changchun, 130022, P. R. China

E-mail: hxzhong@ciac.ac.cn, weilu@ciac.ac.cn, xbzhang@ciac.ac.cn

[b] Dr. N. Zhang, Prof. H. Zhong, Prof. W. Liu, D. Wang, C. Ma, Prof. X. Zhang

School of Applied Chemistry and Engineering

University of Science and Technology of China

No.96, Jinzhai Road, Baohe District, Hefei, Anhui, 230026, P. R. China

[c] Prof. J. Zeng

Shanghai Synchrotron Radiation Facility

Shanghai Advanced Research Institute, Chinese Academy of Sciences

No.239, Zhangheng Road, Pudong new District, Shanghai, 201204, P. R. China

Ning Zhang and Xinyi Liu contribute equally to this work.

Abstract: Developing an active and durable acidic oxygen evolution reaction (OER) catalyst is vital for implementing proton exchange membrane water electrolyzer (PEMWE) in sustainable hydrogen production. However, it remains dauntingly challenging to balance high activity and long-term stability under harsh acidic and oxidizing conditions. Herein, through developing the universal rare-earth participated pyrolysis-leaching approach, we customized the active and long lifespan pseudo-amorphous IrO_x with locally ordered rutile IrO_2 and unique defect sites ($\text{IrO}_x\text{-3Nd}$). $\text{IrO}_x\text{-3Nd}$ achieved a low overpotential of 206 mV and long-term durability of 2200 h with a slow degradation rate of 0.009 mV h^{-1} at 10 mA cm^{-2} , and, more importantly, high efficiency in PEMWE (1.68 V at 1 A cm^{-2} for 1000 h) for practical hydrogen production. Utilizing in-situ characterizations and theoretical calculations, we found that lattice oxygen vacancies (O_v) and contracted Ir-O in locally ordered rutile IrO_2 induced the O_v -modulated lattice oxygen exchange process, wherein thermodynamically spontaneous occupation of surface hydroxyl groups on O_v and effective promotion of O-O coupling and lattice oxygen recovery accounted for enhanced activity and durability. This work underscores the importance of tailor-made local configuration in boosting activity and durability of OER catalyst and different insights into the promotion mechanism.

Introduction

Proton exchange membrane water electrolyzer (PEMWE) is promising for sustainable hydrogen production with high efficiency and purity while storing renewable electricity^[1]. In acidic electrolysis, particularly at the anode side, high energy is required to break strong covalent O-H bonds of water, resulting in slow kinetics of oxygen evolution reaction (OER)^[2]. More seriously, the

acidic and highly oxidative operating conditions exacerbate challenges in developing long-lasting lifespan anode catalysts, which have garnered extensive research interest^[3].

To date, iridium (Ir) oxides are regarded as almost the only appropriate acidic OER catalysts for the practical PEMWE application^[4]. The crystalline rutile IrO_2 , with robust Ir-O bonding and cross-linked $[\text{IrO}_6]$ overall structure, enables the stable OER process through an adsorbate evolution mechanism (AEM), wherein the overpotential is generally high ($\sim 370 \text{ mV}$ at 10 mA cm^{-2})^[5] due to the scaling relationship of various intermediates. Further efforts were devoted to breaking the long-range order of IrO_2 toward active amorphous IrO_x by the chemical and in-situ electrochemical reconstruction way^[6]. The obtained IrO_x possesses the amount of weak corner-shared $[\text{IrO}_6]$ octahedra configurations with fragile Ir-O bonding, which could effectively activate lattice oxygen and induce rapid lattice oxygen participated OER process (LOM)^[7]. Despite high activity, these amorphous IrO_x were inevitably afflicted with severe performance loss caused by insufficient lattice oxygen recovery from these randomly generated O_v and the accompanying Ir dissolution without electron transfer ($\text{Ir}^{\text{III}}_{(\text{oxide})}$ to $\text{Ir}^{3+}_{(\text{aq})}$) over time. Thus, the search for IrO_x with robust $[\text{IrO}_6]$ octahedron connection while active Ir-O remains urgently needed for active and durable OER electrocatalysts.

To this end, we propose that customizing a unique pseudo-amorphous IrO_x with locally ordered rutile IrO_2 with a strong $[\text{IrO}_6]$ octahedron connection and suitable Ir-O could stimulate the active and durable OER process. However, limitations in the synthesis strategy hinder performance exploration and a fundamental understanding of its essential role in OER. Herein, through a rare-earth metal (e.g. Nd, La, Pr, Sm, Eu) participated pyrolysis-leaching method, we developed the long lifespan and

RESEARCH ARTICLE

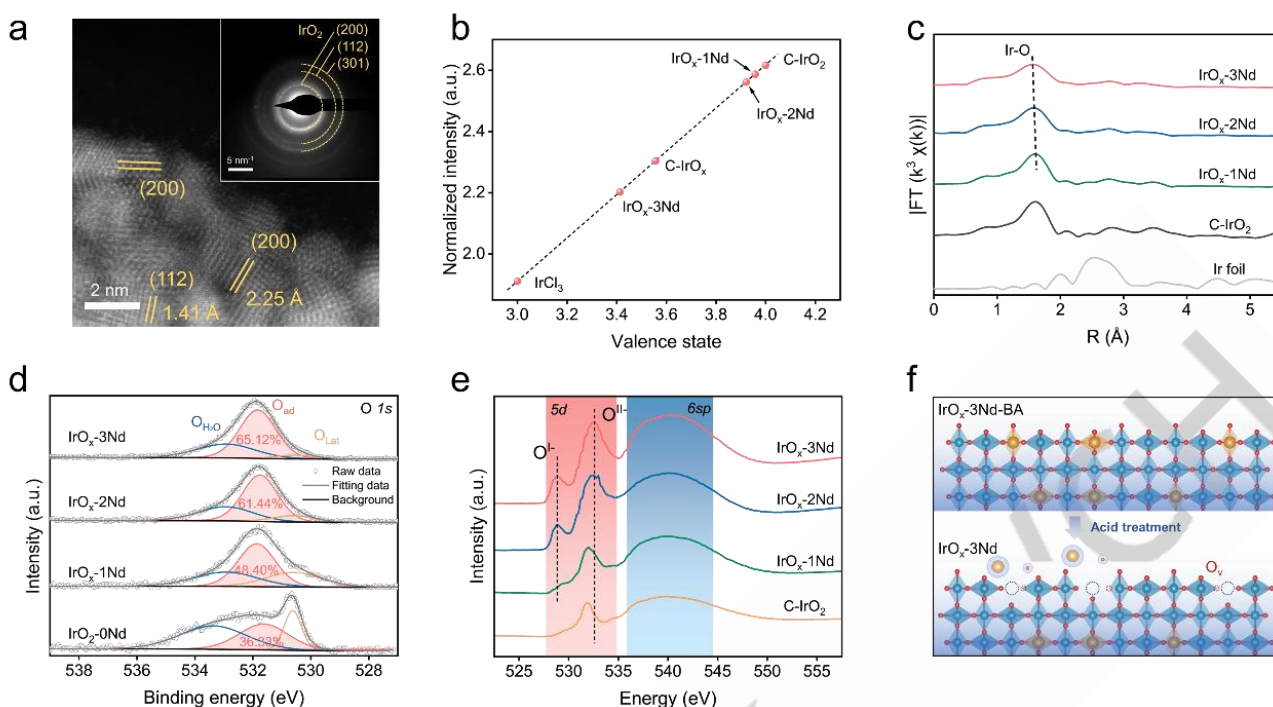


Figure 1. Structural characterization of IrO_x-3Nd and contrasting materials. (a) HAADF-STEM image of IrO_x-3Nd. Inset: the corresponding SAED image. (b) The inferred oxidation states of Ir in IrO_x-3Nd, IrO_x-2Nd, IrO_x-1Nd, and C-IrO_x from Ir L₃-edge XANES. (c) k³-weighted Fourier transforms (FT) of Ir L₃-edge EXAFS spectra of IrO_x-3Nd, IrO_x-2Nd, IrO_x-1Nd, C-IrO₂ and Ir foil. (d) O 1s XPS spectra of IrO_x-3Nd, IrO_x-2Nd, IrO_x-1Nd and IrO₂-0Nd. (e) O K-edge XAS spectra of IrO_x-3Nd, IrO_x-2Nd, IrO_x-1Nd and C-IrO₂. (f) The schematic process for synthesizing IrO_x-3Nd from IrO_x-3Nd-BA via acid treatment.

active pseudo-amorphous IrO_x (IrO_x-3Nd) with locally paracrystalline rutile structure and rich oxygen vacancies (O_v). Thereinto, rare-earth metal promotes the forming of pseudo-amorphous rutile precursors during pyrolysis. Subsequently, acidic leaching of neodymium ions with lattice oxygen ions induces active Ir-O sites and abundant O_v. The obtained IrO_x-3Nd electrocatalyst boosts highly active and durable acidic OER with a low overpotential of 206 mV and long-term durability of 2200 h at 10 mA cm⁻², far superior to the commercial amorphous IrO_x and IrO₂. Notably, IrO_x-3Nd also demonstrates high efficiency (1.68 V at 1 A cm⁻² for 1000 h) in PEMWE devices for practical hydrogen production. Combining in-situ X-ray absorption spectroscopy (XAS) and density functional theory (DFT) calculations analysis, we proposed that IrO_x-3Nd followed the oxygen vacancy-modulated lattice oxygen exchange process (O_v-LOM). Beneficial from the well-regulated local structure and Ir center sites, the spontaneous nucleophilic attack of water molecules and subsequent effectively promoted O-O coupling occurs in this O_v-LOM pathway. Meanwhile, the generation/migration of excess oxygen vacancies was also prevented, and Ir component loss during the OER process was slowed down. This study opens an effective strategy for developing active and long-lifespan OER catalysts and provides a different understanding of its promotion role in acidic OER.

Results and Discussion

Preparation and Characterization of IrO_x-3Nd

A modified sol-gel method is used to synthesize IrO_x-3Nd and its analogs (IrO_x-2Nd, IrO_x-1Nd, and IrO₂-0Nd; see details in Methods). Low Nd content in precursors is related to forming larger particles (Figure S1-2). Notably, IrO₂-0Nd synthesized without Nd precursors presents similar large particle morphology and crystalline structure with commercial IrO₂ (C-IrO₂), which are markedly different from commercial IrO_x without clear crystalline structure (C-IrO_x, Figure S2). IrO_x-3Nd was composed of approximately 2.6 nm nanoparticles as verified by transmission electron microscope (TEM, Figure S1). The clear lattice fringes with the distance of 0.225 nm of (200) facet in high-angle annular dark-field scanning transmission electron microscopy (HAADF-STEM) and the typical diffraction spots in the selected area electron diffraction (SAED) images in **Figure 1a** identified a polycrystalline rutile structure for IrO_x-3Nd. Indeed, no prominent diffraction peaks were observed in the powder X-ray diffraction (XRD, Figure S3) pattern of IrO_x-3Nd. The results verified the critical role of rare-earth metal in successfully preparing IrO_x particles with short-range ordered but long-range disordered structures^[8].

To investigate the electronic structure and local coordination environment of IrO_x-3Nd, X-ray absorption near-edge spectroscopy (XANES) and extended X-ray absorption fine structure (EXAFS) spectra based on synchrotron radiation were collected. XANES results (Figure 1b, details in Figure S4) show that the average Ir valence state of the prepared IrO_x-Nd

RESEARCH ARTICLE

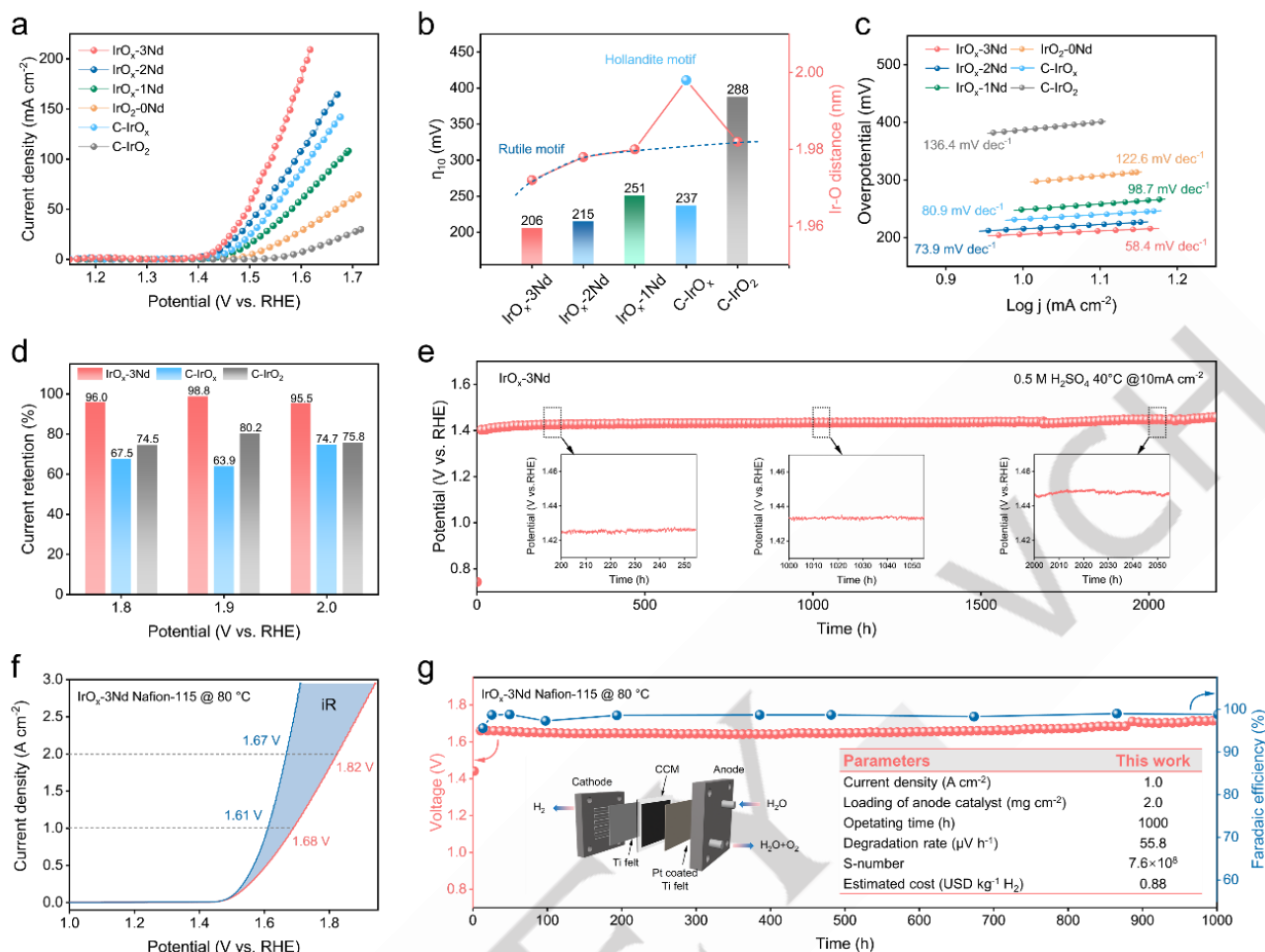


Figure 2. Electrochemical performance of IrO_x-3Nd. (a) LSV curves of IrO_x-3Nd, IrO_x-2Nd, IrO_x-1Nd, IrO_x-0Nd, C-IrO_x and C-IrO₂. (b) Comparison of η_{10} and Ir-O bond length for various electrocatalysts based on EXAFS results. (c) Tafel plots derived from the polarization curves in (a). (d) Current retention of IrO_x-3Nd, C-IrO_x, and C-IrO₂ after chronoamperometry (CA) test at various potentials (1.8 V, 1.9 V, 2.0 V vs. RHE) for 5 h. (e) Chronopotentiometry (CP) test of IrO_x-3Nd in 0.5 M H₂SO₄ at 40 °C at 10 mA cm⁻². Insets are CP curves for 200-255, 1000-1055, and 2000-2055 h. (f) Polarization LSV curve of IrO_x-3Nd in PEMWE at 80 °C. (g) CP test of IrO_x-3Nd in PEMWE at 80 °C at 1 A cm⁻².

electrocatalysts is between +3 and +4^[9]. The oxidation state in IrO_x-Nd is reduced by increasing the Nd content in the precursor. Compared to other counterparts, IrO_x-3Nd presents lower Ir valence state, which is consistent with the lower binding energy of Ir 4f X-ray photoelectron spectroscopy (XPS) spectrum in Figure S5. Besides, IrO_x-3Nd exhibits notably shorter Ir-O bond lengths in the first shell as 1.973 Å based on EXAFS and Raman results (Figure 1c and Figures S7-8). Accordingly, it presents the smallest coordination number (CN) of Ir as 5.77, which means the richer oxygen vacancies (O_v) in IrO_x-3Nd (Table S1). The first and second shell coordination numbers of Ir in IrO_x-3Nd are consistent with the rutile structure, which further confirms its localized rutile structure^[7]. The prevalence of surface oxygen defect species is further indicated by the higher abundance of adsorbed oxygen groups (O_{ad}, 531.8 eV) as 65.12% in O 1s XPS of IrO_x-3Nd (Figure 1d and Table S2)^[10], which are attributed to O_v as confirmed by electron paramagnetic resonance (EPR, Figure S9). In O K-edge XANES (Figure 1d), it was noticed that all IrO_x-Nd electrocatalysts exhibit typical 5d (527-534 eV) and 6sp (535-550 eV) peaks of rutile crystal structure^[11]. The first peak at 528.9 eV is related to

the electron-deficient electrophilic oxygen (O⁺), and the following peak is associated with the lattice oxygen (O²⁻) belonging to the 5d system^[12]. For IrO_x-3Nd, the strong O⁺ peak corresponds to the abundant O_v sites and the increased energy for the O⁺ peak suggests the strengthening Ir-O binding. Oxygen species of IrO_x-3Nd are more active compared to C-IrO₂, as verified by the subsequent H₂ temperature-programmed reduction (H₂-TPR, Figure S10) profile^[13].

Notably, acidic treatment is crucial for synthesizing IrO_x-3Nd with rich defects. Compared to the target IrO_x-3Nd sample, the Ir valence of the IrO_x-3Nd-BA sample (before acidic treatment) is higher than +4, which originates from the doping of Nd³⁺ (Figure S11). After acidic treatment, the Nd content of IrO_x-3Nd is as low as 0.785 wt% according to ICP-AES (Table S3), while the Nd signal is absent in Nd 3d XPS (Figure S12). Combined with DFT calculations, it was concluded that the Nd ion-coupled oxygen dissolution process leads to O_v formation (Figure S13-S15). Accordingly, the construction of O_v in IrO_x-3Nd by surface Nd dissolution during acid treatment was illustrated in Figure 1f. Importantly, this rare-earth ion dissolution method is universal for

RESEARCH ARTICLE

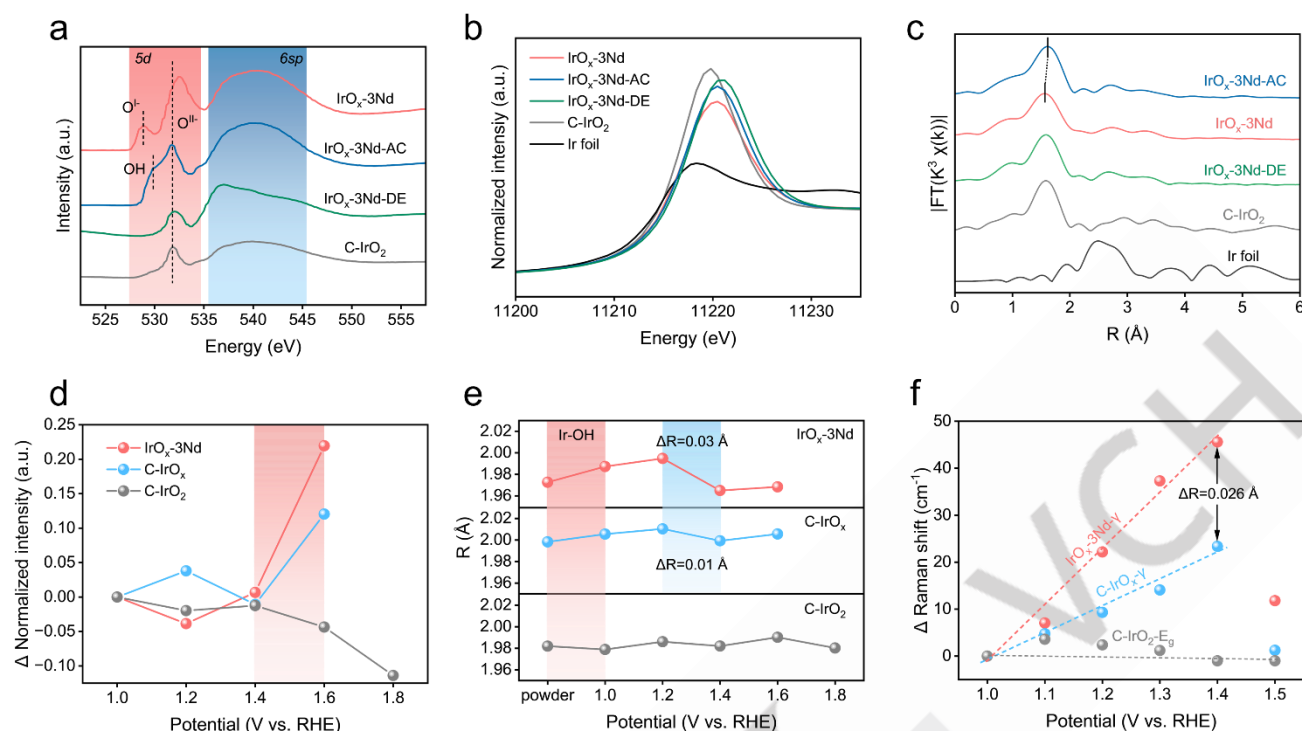


Figure 3. Identification of dynamic active site and in-situ XAFS tests. (a) O K-edge of IrO_x-3Nd, IrO_x-3Nd-AC, IrO_x-3Nd-DE (IrO_x-3Nd after degeneration), and C-IrO₂. (b-c) Ir L₃-edge XANES and FT EXAFS of IrO_x-3Nd, IrO_x-3Nd-AC, IrO_x-3Nd-DE, C-IrO₂, and Ir foil. (d) Differences in white line peaks of IrO_x-3Nd, C-IrO_x, and C-IrO₂ were recorded under various potentials. (e) Ir-O bond distance of IrO_x-3Nd, C-IrO_x, and C-IrO₂ under various potentials. (f) Raman shifts of γ and E_g peak for IrO_x-3Nd, C-IrO_x, and C-IrO₂ electrode under various potentials.

constructing O_v-rich rutile-type pseudo crystal structures of IrO_x (IrO_x-3RE). When using other lanthanide rare earth elements (e.g., La, Pr, Sm, Eu), similar dissolution behavior of IrO_x-3RE was observed during acid treatment (Figure S16-S21). Overall, the rare earth metal participated approach can effectively build the short-range ordered rutile IrO_x with abundant oxygen defects.

Electrocatalytic Performance of IrO_x-3Nd

The acidic OER performances of all samples after electrochemical activation were first evaluated in a three-electrode cell with an O₂-saturated 0.5 M H₂SO₄ electrolyte^[14]. The linear sweep voltammetry (LSV, Figure 2a, and Figure S22) curves reveal that IrO_x-3Nd only requires an overpotential (η_{10}) of 206 mV to reach 10 mA cm⁻². By contrast, IrO_x-2Nd and IrO_x-1Nd show larger overpotentials of 215 and 251 mV, respectively, suggesting the positive role of more vacancies in enhancing OER performance. In contrast, η_{10} of C-IrO_x and C-IrO₂ are 237 and 388 mV (Figure 2b), respectively, which is consistent with the previous reports^[15]. Typically, the OER activity of Ir-based electrocatalysts can be affected by adjusting Ir-O bond length through the compressive or tensile strain of iridium oxide lattice. Despite the amorphous structure, IrO_x-3Nd and C-IrO_x show a distinctly different trend in promoting OER activity (Figure 2b). This implies the different catalytic enhancement mechanisms between IrO_x-3Nd with the short-range ordered rutile structure (Ir-O bond distance: 1.973 Å) and C-IrO_x with hollandite motifs (Ir-O: 1.998 Å). IrO_x-3Nd also presents faster kinetics with a lower Tafel slope of 58.4 mV dec⁻¹ (Figure 2c) than the counterparts and the slightest charge-transfer resistance (R_{ct}) as revealed by

electrochemical impedance spectroscopy (EIS, Figure S23a). The electrochemical active surface area (ECSA, Figure S23b) of IrO_x-3Nd is approximately 1.5 and 181.9 times greater than that of C-IrO_x and C-IrO₂, respectively, further highlighting its advantage of the abundant surface-active sites. Correspondingly, IrO_x-3Nd exhibits a high mass activity of 1.25 A mg_{Ir}⁻¹ at 1.5 V vs. a reversible hydrogen electrode (RHE) (Figure S22d). Chronoamperometry (CA, Figure S24) tests at 1.8, 1.9, and 2.0 V vs. RHE for 5 h show that IrO_x-3Nd maintains higher current retention of 96.0, 98.8, and 95.5% than C-IrO_x and C-IrO₂, suggesting that IrO_x-3Nd is capable of working under high voltages in practical application. When applied for electrocatalytic OER at 10 mA cm⁻² (Figure 2e), IrO_x-3Nd demonstrates only slight potential increases of 20 mV (inset graphs) after 2200 h electrolysis, mainly exceeding the recently reported catalysts (Table S5).

To verify the performance in the operating PEMWE, we assembled a PEMWE device with an IrO_x-3Nd anode electrocatalyst (Figure S25). Deionized water was the feed electrolyte at 80 °C. The current-voltage polarization is shown in Figure 2f. The device achieved the current densities of 1 A cm⁻² and 2 A cm⁻² at output voltage of 1.68 V and 1.82 V (1.61 V and 1.67 V after iR correction), respectively. In addition, PEMWE with IrO_x-3Nd also presents long-term operational stability with a slight voltage increase of only 55.8 mV (55.8 μ V h⁻¹) after 1000 h test at 1 A cm⁻² (Figure 2g and S26). Furthermore, we analyze the stability number (S-number), which is a metric for benchmarking the stability of various electrocatalysts. Benefiting from the

RESEARCH ARTICLE

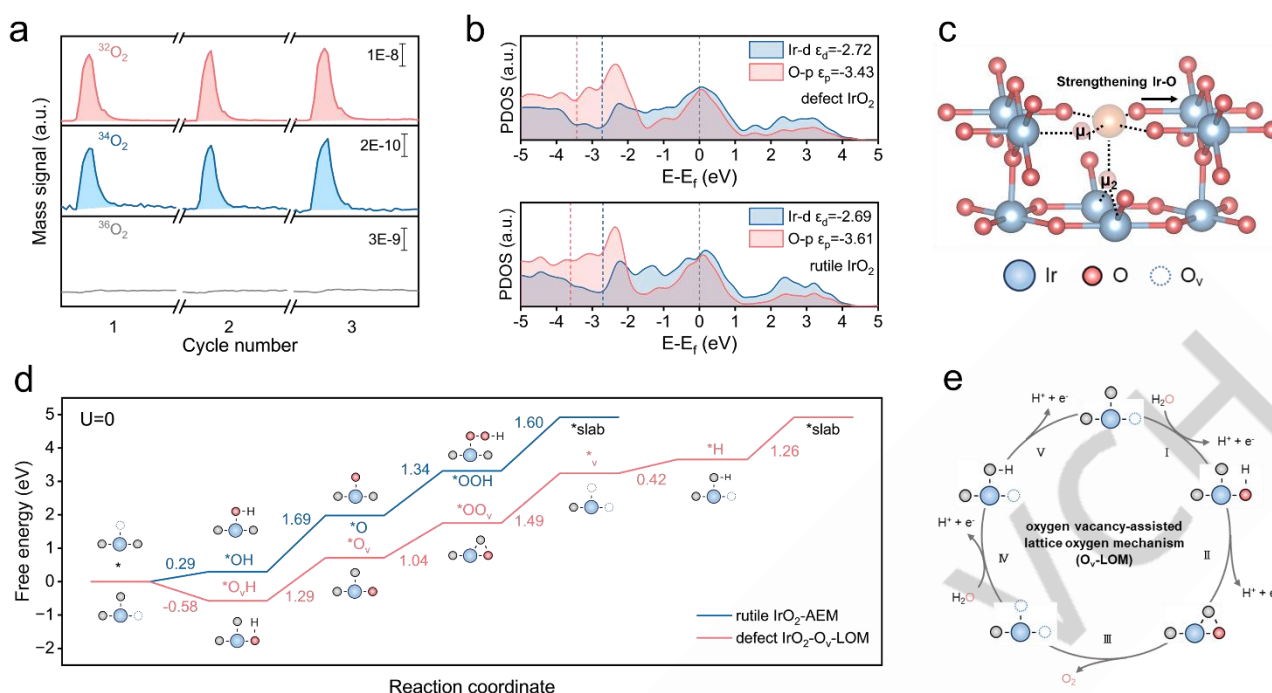


Figure 4. Oxygen vacancy-assisted oxygen exchange mechanism for OER. (a) Online DEMS signals of O_2 products for IrO_x -3Nd. (b) PDOS plots of Nd leaching-induced defect IrO_2 and rutile IrO_2 . (c) Schematic diagrams of the local defect site on Nd leaching-induced IrO_2 . (d) Free-energy diagrams of Nd leaching-induced defect IrO_2 and rutile IrO_2 with AEM and O_V -LOM pathways. (e) Schematic oxygen vacancy-assisted oxygen exchange (O_V -LOM).

intrinsic strength and the rapid mass transfer in the PEMWE configuration, the S-number of IrO_x -3Nd is calculated to be 7.6×10^8 , proving its excellent stability characteristics and long-life potential. It is worth noting that the dissolution rate of Ir in PEMWE is significantly lower than that observed in the three-electrode system thanks to the favorable microenvironment and interface in PEMWE. The estimated cost of hydrogen production using this PEMWE is USD 0.88 per kg H_2 , which goes beyond the 2026 goal of the US Hydrogen Earth shot initiative (USD 2.0 per kg H_2)^[16]. It demonstrates the possibility of enhancing catalyst performance and durability, which are crucial for lowering overall costs. These results further underscore the versatility of IrO_x -3Nd for practical hydrogen production applications.

Identification of Unique Active Site

Both CP and cyclic LSV (Figure S27) tests disclose a distinct electrochemical activation process of IrO_x -3Nd. TEM and HAADF-STEM (Figure S28) images reveal that IrO_x -3Nd undergoes surface amorphization. Thus, IrO_x -3Nd after activation (IrO_x -3Nd-AC) was prepared after electrolysis at 200 mA cm^{-2} for 5 h. In O-K edge XANES of IrO_x -3Nd-AC (Figure 3a), a new characteristic peak of OH species is found at 529.7 eV ^[17]. Its intensity is lower than the dominant bulk contribution of O^{II} . Meanwhile, the disappearance of the O^{II} at 528.9 eV occurs. These results imply that O_V is occupied by oxygen intermediates (e.g., OH species). Besides, the activation also induced a slight increase in the oxidation state of Ir in IrO_x -3Nd-AC than IrO_x -3Nd, as identified by Ir L₃-edge XANES (Figure 3b) results. Moreover, OH adsorption leads to Ir-O bond length elongating from 1.973 \AA to 2.001 \AA based on EXAFS results (Figure 3c and Table S1). Therefore,

hydroxylation contributed to the surface amorphous layer formed during activation.

The in-situ Ir L₃-edge XAFS spectra of IrO_x -3Nd, C- IrO_x , and C- IrO_2 were collected from 1.0 to 1.6 V vs. RHE to investigate the Ir valence changes and structural evolution. Figure 3d, and Figures 29-32 show a rapid increase in the oxidation state of Ir for IrO_x -3Nd and C- IrO_x near the onset potential (1.4-1.6 V vs. RHE), indicating that IrO_x tends to be oxidized compared to rutile C- IrO_2 . Generally, the formation of O-O is sensitive to the oxidation valence state of Ir^[18]. Higher valence Ir favors reducing the activation energy for O coupling toward enhancing reactivity. As a result, it is more conducive to continuously replenishing water molecules in dynamic O_V , thereby improving the overall durability. IrO_x -3Nd exhibits a more significant increase in valence state than C- IrO_x , suggesting that Ir sites of IrO_x -3Nd are more active. The corresponding in-situ EXAFS spectra are shown in Figure S29-32. The variation in fitting Ir-O bond length with various applied potentials is summarized in Figure 3e and revealed a covalency contraction of 0.03 \AA in IrO_x -3Nd before the onset potential (1.0-1.2 V vs. RHE), which is associated with the optimized electronic structure and d-band center^[19]. This observation could arise from the flexible connection of $[IrO_6]$ units with the defective structures in amorphous IrO_x . The shortened Ir-O distance could act as the preferred nucleophilic centers for water molecules, thus facilitating the formation of O-O bonds during OER process^[20]. The structural evolution of IrO_x -3Nd, C- IrO_x , and C- IrO_2 was further revealed by in-situ Raman spectroscopy (Figure S33)^[21]. With the potential increased from open circuit potential (OCP) to 1.4 V vs. RHE (Figure 3f), negative shifts of 44 and 22 cm^{-1} in the Ir-O stretch vibration peak (γ) were observed for IrO_x -3Nd and C-

RESEARCH ARTICLE

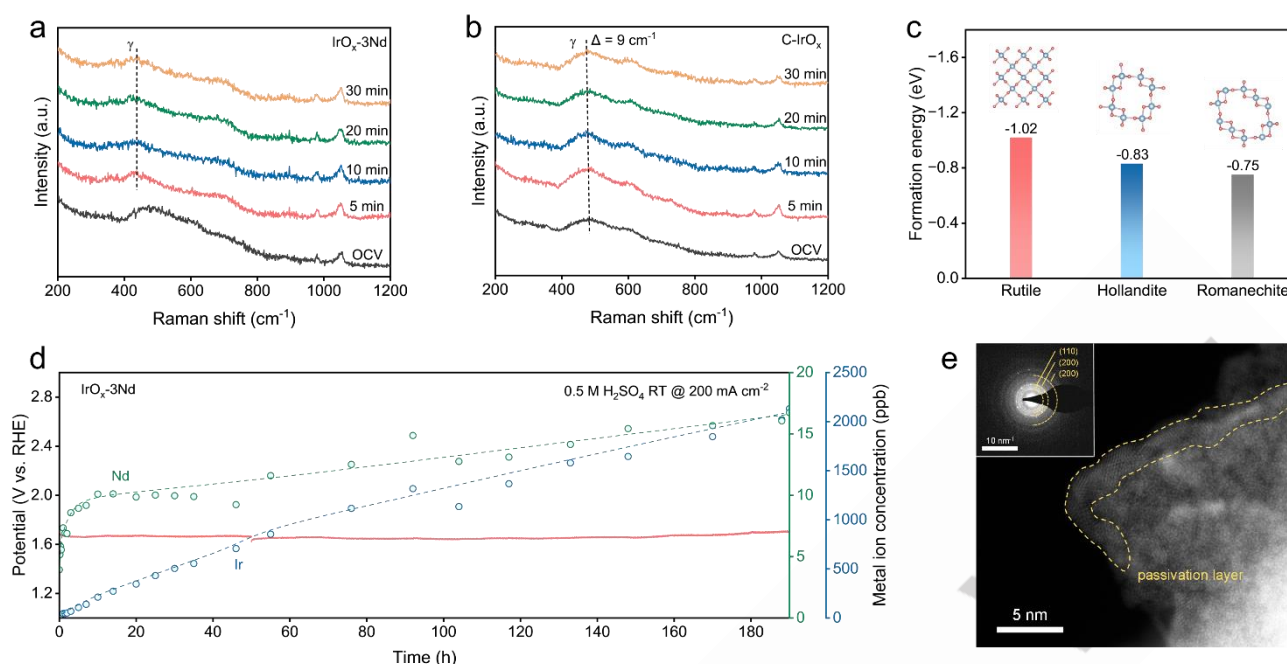


Figure 5. Stability analysis of IrO_x-3Nd. (a, b) Raman spectra of IrO_x-3Nd and C-IrO_x after 0-30 min OER tests. (c) The formation energies of rutile, hollandite and romanechite type IrO₂. (d) CP coupled ICP test and metal (Ir and Nd cations) dissolution ICP results of IrO_x-3Nd at 200 mA cm⁻². (e) HAADF-STEM image of IrO_x-3Nd-DE, inset is corresponding SAED image.

IrO_x, respectively. According to the mathematical correlation between bond length and stretching frequencies for Ir-O bonds, the disparity in bond length between IrO_x-3Nd and C-IrO_x is calculated to be 0.026 Å (detailed explanation in Figure S33). This closely corresponds to the variations of Ir-O in XAFS data at each applied potential. In contrast, Ir-O bond of C-IrO₂ with high structural rigidity remained unchanged^[22].

Insights into Catalytic Reaction Mechanism

Online ¹⁸O isotope-labeling differential electrochemical mass spectrometry (DEMS) of IrO_x-3Nd and C-IrO₂ were analyzed to unveil the reaction pathway. The ¹⁸O-labeled IrO_x-3Nd produces 1.4% ¹⁸O (contained in ¹⁸O¹⁶O) when operating in an H₂¹⁶O electrolyte (Figure 4a and S34a). For comparison, the gas product of ¹⁸O-labeled C-IrO₂ contains 1.0% ¹⁸O (Figure S34b), indicating that the defects induced by Nd leaching will trigger lattice oxygen to participate in the OER cycle process.

Furthermore, DFT calculations were conducted to understand the origin of the promoted OER on defective rutile IrO_x-3Nd compared to rutile C-IrO₂. The model for IrO_x-3Nd was built by removing some Ir atoms and adjacent O-μ₁ atoms on rutile IrO₂ according to experimental results (Figure S35). The most thermodynamically stable (110) facet (lowest surface energy = 0.058 eV Å⁻², Figure S36) among the low-index faces of rutile IrO₂ was chosen as the exposed crystal surface.

According to a partial density of states (PDOS) calculations for the theoretical models of IrO_x-3Nd (Figure 4c) and C-IrO₂, it was found that the electronic structure of IrO_x-3Nd was well optimized. When introducing defects (metal and oxygen vacancies) in rutile IrO₂, its Fermi level moves closer to the computed O 2p-band center (-3.43 eV), and the energy gap (Δε_{p-d}) between the metal (Ir) 5d-band and O-2p band centers was reduced. The increased

p-band center indicates the strengthening covalency of the Ir-O bond in defect IrO₂, which can lower the energy barrier for oxidation of lattice oxygen and then stimulate the occurrence of LOM^[23]. This is consistent with DEMS results. The reduced Δε_{p-d} strengthens the interaction between Ir and O in IrO_x-3Nd, which is beneficial for addressing the issue of Ir-O bond breaking (step III in Figure S37b) during lattice oxygen participation of the conventional LOM process. Besides, the AEM process was impeded due to the weakening adsorption of *OOH intermediates^[24].

Given that the first elementary step in OER involves the adsorption of hydroxyl (*OH), the adsorption energies (E_{ad}) of *OH intermediate were evaluated at each possible active site (Figure S38). The *OH intermediate tends to occupy the Nd leaching-induced oxygen defect sites (O_v-μ₁) with the lowest adsorption energy of -4.70 eV. Thus, the original oxygen vacancy could participate in the oxygen exchange process (designated as O_v-LOM, Figure 4e), which is distinct from conventional AEM and LOM (Figure S37, S39-S40). Namely, O_v on the surface is readily nucleophilic attacked by water molecules under anodic polarization potential. During the initiation process of OER (step I), the facile adsorption of *OH promotes the dissociation of strong covalent bonds (H-OH) in H₂O. The O-O coupling (step III in AEM, step II in LOM, and O_v-LOM) is the most critical step in distinguishing the mechanisms of LOM and O_v-LOM. The newly formed *O intermediates interact with lattice oxygen and thus release oxygen atoms. Note that, as for conventional LOM, O_v sites are randomly generated upon the release of O₂, potentially leading to the dissolution of Ir when the generation rate of O_v exceeds the filling rate^[25]. In O_v-LOM, a low oxygen filling barrier of 0.42 eV was obtained in step VI, owing to the nucleophilic sites of high-valence Ir, contributing to the sufficient recovery of lattice oxygen. Free energy profiles of the overall O_v-LOM and AEM

RESEARCH ARTICLE

processes in defect IrO_2 and rutile IrO_2 , respectively, are shown in Figure 4d. The predicted overpotential of defect IrO_2 is 0.26 V, significantly lower than that of rutile IrO_2 (0.46 V). Moreover, the overpotential of OER via AEM on defect IrO_2 (Figure S41) is predicted as high as 1.30 V with the $\cdot\text{OOH}$ formation. Conversely, highly crystalline rutile IrO_2 favors AEM (overpotential=0.46 V) rather than LOM (overpotential=5.69 V). These results demonstrate that the Nd-participated pyrolysis-leaching strategy is effective in altering the elementary steps and boosts acidic OER activity via a highly active O_v -LOM pathway.

Stability Enhancement Mechanism

Raman spectroscopy was conducted on fresh C-IrO_x and IrO_x -3Nd after different electrolysis durations (Figure 5a and b). Following the first 5 minutes of OER, IrO_x -3Nd underwent structural evolution because of hydroxylation. Then, IrO_x -3Nd remained a more stable rutile structure during the OER process since no apparent shift in the Raman characteristic peaks was observed after hydroxylation. In contrast, the Ir-O stretch vibration peak (γ) in C-IrO_x exhibited a shift of 9 cm^{-1} . This illustrates that IrO_x -3Nd possesses stabilized defect-rich IrO_x framework with abundant vacancies after the dissolution-induced reconstruction. We subsequently compared the formation energy (E_f) of three different iridium oxide configurations in Figure 5c (rutile for IrO_x -3Nd, hollandite for C-IrO_x , and romanechite in Figure S42). The rutile motif has shorter and tight Ir-O bond and a cross-linked shared strong connection structure. In contrast, the hollandite and romanechite motifs experience significant lattice stress and unstable corner-shared connections. Consequently, the rutile motif possesses the lowest E_f of -1.02 eV/atom , indicating its thermodynamically stable and structurally robust property. This suggests that the strengthened Ir-O covalent bonds and locally preserved rutile-like structure synergistically contribute to the simultaneous enhancement of activity and stability.

The specially accelerated durability test under harshly operated conditions was further performed to determine the possible cause of performance degradation for Ir-based electrocatalysts. In CP tests (Fig 5d and Figure S43), IrO_x -3Nd, C-IrO_x , and C-IrO_2 exhibited durability for 190, 13, and 4 h at 200 mA cm^{-2} , respectively. Clearly, IrO_x -3Nd demonstrated higher stability (S-number = 1.59×10^5) than C-IrO_x (S-number = 9.21×10^4). Although Ir dissolution inevitably occurs throughout the entire electrolysis process over time, the increase in the OER potential was absent on IrO_x -3Nd. It is thus deduced that Ir dissolution is not likely the underlying cause for performance degradation. Morphological characterization (Figure 5e and Figure S44) shows the formation of a thin passivation layer on the surface of the designedly degenerative IrO_x -3Nd (IrO_x -3Nd-DE) after CP tests. Combining XAFS (Figure 3a-3c) and XPS (Figure S45), we determined that the passivation layer consists of fully oxidized rutile IrO_2 . Upon deactivation, all IrO_x -3Nd-DE, C-IrO_x -DE, and C-IrO_2 -DE present similar surface Ir species (Figure S46). Thus, the formed passivation layer with long-range ordered rutile structure in the oxidation condition could be the leading cause of OER performance deactivation of Ir-based electrocatalysts. Even though approximately 49.7% of Ir in IrO_x -3Nd was dissolved (Table S6), IrO_x -3Nd also maintains relatively stable electrolysis.

This is because Nd-leaching-induced highly active sites can afford the sufficient recovery of the lattice oxygen, deliver the benchmark current density at lower operated voltage, and bypass the formation of the passivation layer under high overpotential during OER.

Conclusion

In summary, we developed a universal rare-earth metal participated pyrolysis-leaching strategy to build the long-range disordered IrO_x catalyst with a short-range ordered rutile motif and unique defect sites. The optimized IrO_x -3Nd enables an active and durable acidic OER process with a low overpotential of 206 mV and 2200 h durability at 10 mA cm^{-2} . Moreover, it also afforded excellent stability up to 1000 h at 1 A cm^{-2} with 1.68 V cell voltage in PEMWE. Using in-situ characterization and theoretical analysis, we proposed that IrO_x -3Nd promotes oxygen generation via an oxygen vacancy-assisted LOM mechanism (O_v -LOM). The spontaneous adsorption of surface hydroxyl groups and the facilitated proton-electron transfer process contribute to the enhanced catalytic performance. The slower dissolution of Ir cations and the accelerated recovery of lattice oxygen during electrochemical reactions sustained the high durability. This study offers valuable references to boost and stabilize the acidic OER and clarify the mechanism behind the enhanced activity of multi-component iridium-based catalysts.

Supporting Information

Supplemental information can be found in *Supporting Information.docx* (Supplemental experimental procedures, Figures S1-46 and Tables S1-8).

Acknowledgements

This work was supported by the National Key R&D Program of China (2022YFB4002201), the National Natural Science Foundation of China (52273277 and 52171194), Jilin Province Science and Technology Development Plan Funding Project (SKL202302039 and 20230201150GX) and Youth Innovation Promotion Association CAS (2021223). These authors thank the staff of beamline BL13SSW at the Shanghai Synchrotron Radiation Facility and beamlines 1W1B at the Beijing Synchrotron Radiation Facility (BSRF) for experiment support. H.X. Zhong acknowledges funding from the National Natural Science Foundation of China Outstanding Youth Science Foundation of China (Overseas).

Keywords: Hydrogen production • proton exchange membrane water electrolyzer • oxygen evolution reaction • pseudo-amorphous IrO_x • electrocatalysis • oxygen vacancies

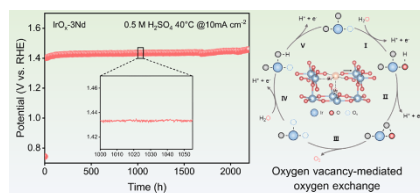
- [1] a L. Chong, G. Gao, J. Wen, H. Li, H. Xu, Z. Green, J. D. Sugar, A. J. Kropf, W. Xu, X. M. Lin, H. Xu, L. W. Wang, D. J. Liu, *Science* **2023**, 380, 609-616; b M. F. Lagarde, A. Grimaud, *Nat. Mater.* **2020**, 19, 1140-1150;

RESEARCH ARTICLE

- c S. Hao, H. Sheng, M. Liu, J. Huang, G. Zheng, F. Zhang, X. Liu, Z. Su, J. Hu, Y. Qian, L. Zhou, Y. He, B. Song, L. Lei, X. Zhang, S. Jin, *Nat. Nanotechnol.* **2021**, *16*, 1371-1377.
- [2] a C. Lin, J.-L. Li, X. Li, S. Yang, W. Luo, Y. Zhang, S.-H. Kim, D.-H. Kim, S. S. Shinde, Y.-F. Li, Z.-P. Liu, Z. Jiang, J.-H. Lee, *Nat. Catal.* **2021**, *4*, 1012-1023; b A. Grimaud, A. Demortière, M. Saubanère, W. Dachraoui, M. Duchamp, M.-L. Doublet, J.-M. Tarascon, *Nat. Energy* **2016**, *2*, 16189; c J. Gao, H. Tao, B. Liu, *Adv. Mater.* **2021**, *33*, e2003786; d H. Wang, X. Han, L. Zhang, K. Wang, R. Zhang, X. Wang, S. Song, H. Zhang, *Fundam. Res.* **2023**, *3*, 356-361.
- [3] a C. Rong, K. Dastafkan, Y. Wang, C. Zhao, *Adv. Mater.* **2023**, *35*, e2211884; b S. Geiger, O. Kasian, M. Ledendecker, E. Pizzutillo, A. M. Mingers, W. T. Fu, O. Diaz-Morales, Z. Li, T. Oellers, L. Fruchter, A. Ludwig, K. J. J. Mayrhofer, M. T. M. Koper, S. Cherevko, *Nat. Catal.* **2018**, *1*, 508-515; c T. Li, O. Kasian, S. Cherevko, S. Zhang, S. Geiger, C. Scheu, P. Felfer, D. Raabe, B. Gault, K. J. J. Mayrhofer, *Nat. Catal.* **2018**, *1*, 300-305.
- [4] a H. N. Nong, L. J. Falling, A. Bergmann, M. Klingenhof, H. P. Tran, C. Spori, R. Mom, J. Timoshenko, G. Zichittella, A. Knop-Gericke, S. Piccinin, J. Perez-Ramirez, B. R. Cuenya, R. Schlögl, P. Strasser, D. Teschner, T. E. Jones, *Nature* **2020**, *587*, 408-413; b H. Sun, X. Xu, H. Kim, W. Jung, W. Zhou, Z. Shao, *Energy Environ. Mater.* **2022**, *5*, e12441.
- [5] a X. Wang, H. Zhong, S. Xi, W. S. V. Lee, J. Xue, *Adv. Mater.* **2022**, *34*, e2107956; b L. Li, P. Wang, Q. Shao, X. Huang, *Adv. Mater.* **2021**, *33*, e2004243; c Z. Shi, Y. Wang, J. Li, X. Wang, Y. Wang, Y. Li, W. Xu, Z. Jiang, C. Liu, W. Xing, J. Ge, *Joule* **2021**, *5*, 2164-2176; d J. Ni, Z. Shi, Y. Wang, J. Yang, H. Wu, P. Wang, M. Xiao, C. Liu, W. Xing, *eScience* **2025**, *2*, 100295.
- [6] a L. An, C. Wei, M. Lu, H. Liu, Y. Chen, G. G. Scherer, A. C. Fisher, P. Xi, Z. J. Xu, C. H. Yan, *Adv. Mater.* **2021**, *33*, e2006328; b S. Chen, S. Zhang, L. Guo, L. Pan, C. Shi, X. Zhang, Z. F. Huang, G. Yang, J. J. Zou, *Nat. Commun.* **2023**, *14*, 4127; c Q. Qin, H. Jang, Y. Wang, L. Zhang, Z. Li, M. G. Kim, S. Liu, X. Liu, J. Cho, *Adv. Energy Mater.* **2020**, *11*, 2003561; d L. C. Seitz, C. F. Dickens, K. Nishio, Y. Hikita, J. Montoya, A. Doyle, C. Kirk, A. Vojvodic, H. Y. Hwang, J. K. Nørskov, T. F. Jaramillo, *Science* **2016**, *353*, 1011-1014.
- [7] M. Elmaalouf, M. Odziomek, S. Duran, M. Gayard, M. Bahri, C. Tard, A. Zitolo, B. Lassalle-Kaiser, J. Y. Piquemal, O. Ersen, C. Boissiere, C. Sanchez, M. Giraud, M. Faustini, J. Peron, *Nat. Commun.* **2021**, *12*, 3935.
- [8] H. N. Nong, T. Reier, H.-S. Oh, M. Gliech, P. Paciok, T. H. T. Vu, D. Teschner, M. Heggen, V. Petkov, R. Schlögl, T. Jones, P. Strasser, *Nat. Catal.* **2018**, *1*, 841-851.
- [9] J. Gao, C. Q. Xu, S. F. Hung, W. Liu, W. Cai, Z. Zeng, C. Jia, H. M. Chen, H. Xiao, J. Li, Y. Huang, B. Liu, *J. Am. Chem. Soc.* **2019**, *141*, 3014-3023.
- [10] F. Frati, M. Hunault, F. M. F. de Groot, *Chem. Rev.* **2020**, *120*, 4056-4110.
- [11] a Z. Shi, J. Li, J. Jiang, Y. Wang, X. Wang, Y. Li, L. Yang, Y. Chu, J. Bai, J. Yang, J. Ni, Y. Wang, L. Zhang, Z. Jiang, C. Liu, J. Ge, W. Xing, *Angew. Chem. Int. Ed. Engl.* **2022**, *61*, e202212341; b Z. Shi, J. Li, Y. Wang, S. Liu, J. Zhu, J. Yang, X. Wang, J. Ni, Z. Jiang, L. Zhang, Y. Wang, C. Liu, W. Xing, J. Ge, *Nat. Commun.* **2023**, *14*, 843.
- [12] Y. Wang, R. Yang, Y. Ding, B. Zhang, H. Li, B. Bai, M. Li, Y. Cui, J. Xiao, Z. S. Wu, *Nat. Commun.* **2023**, *14*, 1412.
- [13] J. Shan, C. Ye, S. Chen, T. Sun, Y. Jiao, L. Liu, C. Zhu, L. Song, Y. Han, M. Jaroniec, Y. Zhu, Y. Zheng, S. Z. Qiao, *J. Am. Chem. Soc.* **2021**, *143*, 5201-5211.
- [14] a E. Willinger, C. Massue, R. Schlögl, M. G. Willinger, *J. Am. Chem. Soc.* **2017**, *139*, 12093-12101; b B. Lu, C. Wahl, R. dos Reis, J. Edgington, X. K. Lu, R. Li, M. E. Sweers, B. Ruggiero, G. T. K. K. Gunasooriya, V. David, L. C. Seitz, *Nat. Catal.* **2024**, *7*, 868-877.
- [15] Y. Wang, X. Lei, B. Zhang, B. Bai, P. Das, T. Azam, J. Xiao, Z. S. Wu, *Angew. Chem. Int. Ed. Engl.* **2024**, *63*, e202316903.
- [16] Y. Wang, M. Zhang, Z. Kang, L. Shi, Y. Shen, B. Tian, Y. Zou, H. Chen, X. Zou, *Nat. Commun.* **2023**, *14*, 5119.
- [17] N. Diklić, A. H. Clark, J. Herranz, D. Aegerter, J. S. Diercks, A. Beard, V. A. Saveleva, P. Chauhan, M. Nachtegaal, T. Huthwelker, D. Lebedev, P. Kayser, J. A. Alonso, C. Copéret, T. J. Schmidt, *ACS Catal.* **2023**, *13*, 11069-11079.
- [18] a Y. Wen, P. Chen, L. Wang, S. Li, Z. Wang, J. Abed, X. Mao, Y. Min, C. T. Dinh, P. Luna, R. Huang, L. Zhang, L. Wang, L. Wang, R. J. Nielsen, H. Li, T. Zhuang, C. Ke, O. Voznyy, Y. Hu, Y. Li, W. A. Goddard, III, B. Zhang, H. Peng, E. H. Sargent, *J. Am. Chem. Soc.* **2021**, *143*, 6482-6490; b J. J. Velasco-Velez, E. A. Carbonio, C. H. Chuang, C. J. Hsu, J. F. Lee, R. Arrigo, M. Havecker, R. Wang, M. Plodinec, F. R. Wang, A. Centeno, A. Zurutuza, L. J. Falling, R. V. Mom, S. Hofmann, R. Schlögl, A. Knop-Gericke, T. E. Jones, *J. Am. Chem. Soc.* **2021**, *143*, 12524-12534.
- [19] H. Gao, Z. Xiao, S. Du, T. Liu, Y. C. Huang, J. Shi, Y. Zhu, G. Huang, B. Zhou, Y. He, C. L. Dong, Y. Li, R. Chen, S. Wang, *Angew. Chem. Int. Ed. Engl.* **2023**, *62*, e202313954.
- [20] a S. Czioska, A. Boubnov, D. Escalera-López, J. Geppert, A. Zagalskaya, P. Röse, E. Saraçi, V. Alexandrov, U. Krewer, S. Cherevko, J.-D. Grunwaldt, *ACS Catal.* **2021**, *11*, 10043-10057; b J. Xu, H. Jin, T. Lu, J. Li, Y. Liu, K. Davey, Y. Zheng, S. Z. Qiao, *Sci. Adv.* **2023**, *9*, eadh1718.
- [21] F. Zhao, B. Wen, W. Niu, Z. Chen, C. Yan, A. Selloni, C. G. Tully, X. Yang, B. E. Koel, *J. Am. Chem. Soc.* **2021**, *143*, 15616-15623.
- [22] A. V. Korotcov, Y. S. Huang, K. K. Tiong, D. S. Tsai, *J. Raman Spectrosc.* **2007**, *38*, 737-749.
- [23] H. Zhong, Q. Zhang, J. Yu, X. Zhang, C. Wu, H. An, Y. Ma, H. Wang, J. Zhang, Y. W. Zhang, C. Diao, Z. G. Yu, S. Xi, X. Wang, J. Xue, *Nat. Commun.* **2023**, *14*, 7488.
- [24] X. Rong, J. Parolin, A. M. Kolpak, *ACS Catal.* **2016**, *6*, 1153-1158.
- [25] L. She, G. Zhao, T. Ma, J. Chen, W. Sun, H. Pan, *Adv. Funct. Mater.* **2021**, *32*, 2108465.

RESEARCH ARTICLE

Entry for the Table of Contents



A strategy to enhance OER activity and durability by tailoring pseudo-amorphous IrO_x with a locally ordered rutile structure and unique defects is developed. The generated defect-active sites afford the oxygen vacancy-mediated oxygen exchange process with favorable O-O bonding and efficient lattice oxygen recovery, presenting an 2200 h stability at 10 mA cm⁻² and 1.68 V at 1 A cm⁻² for 1000 h in proton exchange membrane water electrolyzers.